Bright cavity solitons in metamaterials with internal resonances

A. V. Yulin,[1] V. Kuzmiak,[2] and S. Eyderman[2]
[1]*Department of Nanophotonics and Metamaterials, ITMO University 197101, Kronverksky Avenue 49, St. Petersburg, Russian Federation*
[2]*Institute for Photonics and Electronic of Czech Academy of Science, Chaberska 57, 182 51, Praha 8, Czech Republic*
(Received 3 December 2014; published 16 June 2015)

We explore the formation of bright dissipative solitons in cavities with built-in nonlinear resonators. The solitons in such systems are studied both analytically and numerically. We have found a different kind of bright soliton which emerges due to an intrinsic bistability of the system. The solitonic structures have discontinuity in the plasmonic part of the polaritonic field and exist due to an intrinsic multiplicity of the solution for the plasmonic resonators density. The solutions may have two profoundly different localization scales, referred to as single- and dual-core solitons. We found that the bifurcation diagrams associated with dissipative solitons reveal the existence either a single- or a dual-core soliton depending on the intensity of the fields in a cavity. It was established that the solitons of both kinds can be dynamically stable and thus can be observed experimentally. A physical system for which the predicted phenomena may occur is described in terms of the effective medium model and verified numerically.

DOI: 10.1103/PhysRevA.91.063820 PACS number(s): 42.65.Tg, 05.45.Yv, 42.65.Pc

I. INTRODUCTION

The systems consisting of a planar cavity with built-in resonators of different physical nature attracted a great deal of attention recently. For example, the photons confined in the cavity can strongly interact with the resonators embedded in it when the cutoff frequency of the cavity is close to the frequency of the intrinsic resonances. Strong coupling between the photons trapped in the cavity and the resonator modes gives rise to many interesting nonlinear phenomena in such systems. One of the most intensively studied systems belonging to polaritonic structures is a semiconductor microcavity with strong exciton-photon interaction [1]. An intensive investigation of the phenomena associated with the strong and fast nonlinear response of microcavity exciton-polaritons has led to the discovery of Bose-Einstein condensation of polaritons [2,3] that occurs due to the small effective mass of its photon component at temperatures much higher than those needed for condensation of atomic gases. It has been demonstrated that the polaritons exhibit superfluidity [4,5] and support the formation of the vortices [6,7]. Recent discoveries also include the observation of bistability [4,8], polarization multistability [9–12], and parametric four-wave mixing [9–13].

Since the polaritonic systems are intrinsically non-Hamiltonian, they are in the photonics context often referred to as dissipative, in which losses are important and the presence of an external energy supply is implicitly assumed [14–16]. Dissipative-matter solitons in exciton condensates were reported in Ref. [17] and dissipative dark and bright polariton solitons in microcavities were discussed in [18–20].

In exciton-polariton systems the internal resonances imply a rich variety of the effects associated with their dispersion (diffraction) properties. Namely, it has been demonstrated that in periodic and discrete systems different kinds of Bragg solitons can be formed [21]. Bragg solitons may possess unusual properties; for example, it was predicted that moving Bragg solitons usually emit transitional radiation [22]. A special family of midband Bragg solitons was considered in [23] and the multicore discrete solitons were reported in [24]. The Bragg systems may have both the focusing and the defocusing nonlinearities and the richness of their dispersion properties stems from the resonant coupling of the cavity modes.

A considerable effort has been devoted recently to the investigation of light-matter coupling phenomena in polaritonic photonic crystal structures with complex unit cells containing nanostructured semiconductors or metallic materials. The attractiveness of such structures stems from their ability to control electronic and photonic resonances simultaneously and thus they may offer new possibilities for tailoring the light-matter interaction.

Resonant interaction is a powerful tool to modify material properties. For example, it is convenient to employ either exciton resonances or plasmonic ones, because the wavelength of plasmons (excitons) is much shorter then the wavelength of the mode in a host material and therefore *plasmonic nanoparticles can be considered as localized weakly interacting resonators embedded into a host dielectric*. Among the most prominent examples of such polaritonic crystal structures belong periodically modulated metal surfaces, including surface corrugation [25–28] and hole arrays [29] and regular arrangements of individual metal nanoparticles on dielectric substrates [30]. Novel properties and new effects observed in these structures, such as large photonic band gaps [25], extraordinary light transmission properties through arrays of subwavelength holes [29], negative refraction [31], and strong coupling effects between electronic and photonic resonances [32,33], provide insight into a different class of light-matter coupling phenomena.

The cavities with built-in resonance inclusions can have two profoundly different scales: Assuming that direct interaction between the resonators is weak, the diffraction of the cavity mode is much stronger than the diffraction in the resonators mode. Simultaneously, nonlinear properties of the systems are determined mainly by the resonators, which may lead to the formation of unusual solitons possessing cores of two very different characteristic sizes. These solitons are in a certain sense analogous to Abrikosov vortices in superconductors of the second kind, where the characteristic size of variation of magnetic field is much larger than the characteristic size of the variation of the order parameter.

In this paper we consider the systems with the focusing nonlinearity and intrinsic resonances provided by subwavelength built-in resonators. Specifically, we employ plasmon-polariton systems where metallic nanoparticles yield intrinsic plasmonic resonance. Such structures can support hybrid light-matter excitations (plasmon-polaritons) and they to a large extent resemble the exciton-polariton systems. The advantage of the plasmon-polaritons stems from the fact that the focusing nonlinearity can easily be achieved in these systems.

As an envisaged physical realization of this system we suggest a planar Fabry-Pérot cavity filled with a nonlinear medium in which metallic nanoparticles are embedded. In general, such a system offers a possibility to investigate the fundamental optical effects originating from the resonant excitation of localized surface plasmons and optical waveguide modes. Hereafter we refer to the field associated with the optical waveguide mode as a cavity mode and the field of the built-in resonators as a resonators mode. We focus on phenomena associated with the formation and the dynamics of dissipative solitons in a cavity with internal plasmonic resonances. The nonlinearity in the system is primarily due to the internal plasmonic resonators arising from the field enhancement in the vicinity of the metallic surface, while the diffraction is mainly attributed to the cavity mode.

The aim of the present paper is to investigate bright dissipative solitons possessing two cores with different characteristic scales and which bifurcate from their conservative counterparts in the media with focusing nonlinearity. The feasibility of plasmon-polariton systems stems from the fact that they make it possible to combine strong light-matter coupling and intrinsic resonators with focusing nonlinearity.

The paper is organized as follows. In Sec. II we describe a simple theoretical model based on the effective medium that makes it possible to allows determining the relevant material and geometrical parameters of the realistic cavity with built-in resonators. A detailed description of the analytical model and its numerical verification is presented in the Appendix. In Sec. II we present a standard model which describes a cavity with built-in resonators in terms of the coupled differential equations for the fields $\mathcal{E}(x,t)$ and $\Psi(x,t)$ associated with the cavity and resonators, respectively. Within the approximation based on neglecting the nonlinear and dissipative terms we determine the dispersion relation for linear excitations which consists of the two branches.

In Sec. IV we consider stationary one-dimensional solutions in a one-dimensional conservative case when the problem can be analyzed on a two-dimensional phase plane. By means of numerical simulations we compute the results for the dissipative solitons and we show that they can have cores with very distinct sizes.

In Sec. IV A we study the structural and dynamical stability of the dissipative solitons. The dynamics and adiabatic decay of the quasisolitons affected by small losses in the absence of the pump are considered in Sec. IV B. In Sec. V we consider stationary dissipative cavity solitons with a resonant pump and we explore properties associated with bifurcation diagrams that support either single-core or double-core solitons depending on the intensity of the fields. In the Conclusion we summarize the results obtained and discuss the existence of double-core solitons in analogy to superconductors of the second kind.

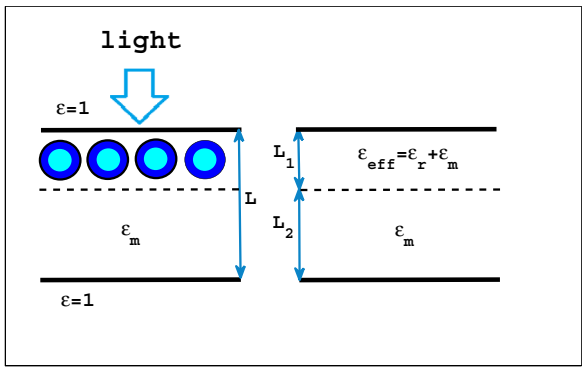

FIG. 1. (Color online) Schematic description of the homogenization model for a FP cavity with Au-coated nanoparticles with an active core. Au coating is indicated by a dark-colored ring, while a bright-colored inner circle corresponds to an active core fabricated from rare-earth-ion-doped silica.

II. HOMOGENIZATION MODEL

In this section we propose a simple theoretical model based on the effective medium approach which describes the system consisting of the cavity with metallic nanoparticles in terms of the frequency-dependent effective dielectric constant $\epsilon_{\text{eff}}(\omega)$. Specifically, we consider a Fabry-Pérot (FP) cavity filled with SiO_2 glass characterized by the dielectric function $\epsilon_m = 2.1$ in which Au nanoparticles are embedded; see Fig. 1. The interior of the cavity is described by an effective permittivity $\epsilon_{\text{eff}}(\omega) = \epsilon_m + f\epsilon_{rm}(\omega)$, where the filling fraction $f = L_1/(L_1 + L_2)$ is given by the ratio between the widths of two layers depicted in Fig. 1. The layers are characterized by the dielectric functions $\epsilon_{rm}(\omega) = \epsilon_m + \epsilon_r(\omega)$ and ϵ_m, where $\epsilon_r(\omega)$ accounts for the resonant behavior of the metallic nanoparticles that is described by Lorentz-Drude-like form dielectric function in the form

$$\epsilon_r(\omega) = \epsilon_0 - \frac{\sigma_c}{\omega^2 - \Omega^2 + i\gamma\omega}, \tag{1}$$

where Ω is the localized surface plasmon resonance (LSPR) frequency, σ_c is the coupling strength between the cavity mode and a surface plasmon mode, ϵ_0 corresponds to the dielectric susceptibility of the LSPR frequency, and γ denotes dissipation of the surface plasmon mode. A key idea of the homogenization model is based on the assumption that the parameters σ_c and γ can be determined from comparison of the transmission, reflection, and extinction coefficients associated with the system described by an effective medium model and the results of the finite-difference time-domain (FDTD) numerical calculations of the corresponding three-dimensional (3D) structure containing a FP resonator with metallic nanoparticles.

To do so, we first employed the results obtained from the FDTD numerical calculations for the system consisting of Au nanoparticles embedded in a FP cavity to extract the values for the parameters σ_c and γ. By using the latter parameters in evaluation of an effective permittivity $\epsilon_{\text{eff}}(\omega)$ we found that the size of the resulting width of the resonance associated with the cavity significantly exceeds the critical size which yields a sufficiently large value of the resonator Q-factor($\sim$50)

that is required to support the existence of the dissipative solitons. To overcome this intrinsic limitation arising from ohmic, we examined a modified configuration, where lossy Au nanoparticles are replaced with coated Ag nanoparticles with active cores made of rare-earth-ion-doped silica. We have verified a feasibility of such system by using a computational approach for simulation of plasmonic nanoparticles [34,35] that allows calculating the effective scattering, extinction, and absorption cross sections of an active nanoparticle. We have shown that by applying a sufficiently high-power one obtains significantly enhanced effective scattering cross section, which, in turn, makes it possible to achieve a sharp cavity resonance corresponding to sufficiently large value of the Q factor. Therefore, the cavity with active nanoparticles may be considered as a feasible system where the phenomena associated with the formation and dynamics of the dissipative solitons described below might be observed experimentally. We note that SiO_2 which fills the cavity is a passive medium unlike that that of a rare-earth-ion-doped silica used in metal-coated nanoparticles with active cores. An undoped SiO_2 in which the nanoparticles within FP cavity are embedded represents a nonlinear medium and it supports the existence of the nonlinear states in the cavity. A more detailed description of the analytical model and its numerical verification is presented in the Appendix.

III. MODEL EQUATION

Below we focus on the microcavity model which describes a cavity with built-in resonators in the slow varying amplitude approximation

$$\partial_t \mathcal{E} - i\left(\partial_x^2 + \partial_y^2\right)\mathcal{E} + (\gamma_1 - i\Delta_1)\mathcal{E} = i\Psi - iE_p, \qquad (2)$$

$$\partial_t \Psi - i\sigma\left(\partial_x^2 + \partial_y^2\right)\Psi + (\gamma_2 - i\Delta_2 - i|\Psi|^2)\Psi = i\mathcal{E}, \quad (3)$$

where $\mathcal{E} = \mathcal{E}(x,t)$ is the complex amplitude of the cavity mode, $\Psi = \Psi(x,t)$ is the amplitude of the field of nonlinear resonators, γ_1 and γ_2 are the losses for the cavity and the resonator modes, respectively, Δ_1 and Δ_2 are the detunings of the cutoff frequency of the cavity and the frequency of the internal resonance with respect the pump frequency, E_p is the pump field, and σ is the coefficient describing the diffraction of the resonators mode. We assume that the pump is spatially uniform in terms of both the amplitude and the phase. We note that the effects of the dissipation, presence of the internal pump, and inclusion of a compensating gain are important for the experimental realization. We choose the pump in the form of a driving force which stands on the right-hand side of the Eq. (2). It corresponds to the cavity driven resonantly by external coherent light at normal incidence.

We first study the properties of the linear waves in the system. The linear excitations can be characterized by their dispersion characteristics. By looking for the solution in the form $\mathcal{E}, \Psi \sim e^{-i\omega t + ikx}$ and by neglecting the dissipative and nonlinear terms we obtain the following dispersion relation $\omega(k)$ for the dispersive waves in the system

$$\omega_{\pm} = \frac{(1+\sigma)k^2 - 2\Delta \pm \sqrt{[\delta + (\sigma-1)k^2]^2 + 4}}{2}, \qquad (4)$$

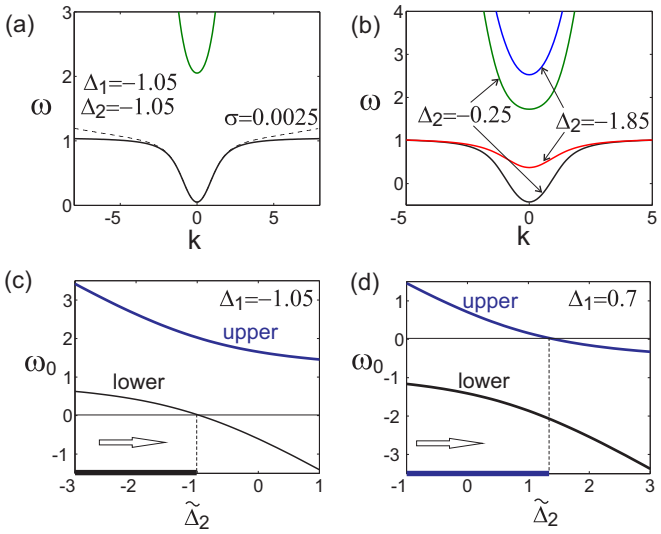

FIG. 2. (Color online) The dispersion characteristics of the cavity with internal plasmonic resonances is shown in panel (a) for $\Delta_1 = -1.05$, $\Delta_2 = -1.05$. The solid line indicates the dispersion for $\sigma = 0$, while the dashed line corresponds to $\sigma = 0.0025$. Panel (b) shows the dispersion characteristics for the constant $\Delta_1 = -1.05$ and variable Δ_2. The dependencies of the frequency of the spatially uniform backgrounds with zero-wave vectors vs $\tilde{\Delta}_2$ are shown in panels (c) and (d) for $\Delta_1 = 0.7$ and $\Delta_1 = -1.05$, respectively.

where $\Delta = \frac{\Delta_1 + \Delta_2}{2}$ and $\delta = \Delta_1 - \Delta_2$. The parameter Δ controls only the shift of the dispersion characteristics in respect to the chosen reference frequency, while δ defines the detuning between the plasmon and cavity resonances and thus affects the shape of the dispersion characteristics.

The interaction between the waveguide cavity mode and plasmonic resonators gives rise to lower and upper plasmon-polariton branches which form the dispersion relation shown in Figs. 2(a) and 2(b). In the absence of direct interaction between the resonators $\sigma = 0$, there exists a gap between the lower and the upper branches of the dispersion characteristics. It is important to note that the gap closes for any finite σ, i.e., when the resonators interact between each other through their evanescent fields.

Now let us consider spatially uniform nonlinear states in the conservative limit and show that these states can be bistable. The solutions can be expressed in the form of plane waves $\mathcal{E}, \Psi \sim e^{-i\omega t + ikx}$. In the absence of pump $E_p = 0$ the equation for the frequency of these backgrounds coincides with the dispersion relation (4), where the detuning Δ_2 has to be substituted with the effective detuning $\tilde{\Delta}_2 = \Delta_2 + \rho^2$ accounting for the nonlinear correction of the resonant frequency, where ρ is the amplitude of field Ψ of the background $\Psi = \rho e^{i\omega t - ikx}$. Correspondingly, the backgrounds possess the structures of the linear modes albeit calculated for the effective detuning $\tilde{\Delta}_2$. Thus, we can distinguish the backgrounds having the structure of the upper and the lower polariton modes.

We can calculate how the frequency of the spatially uniform state depends on the effective detuning. These dependencies are shown in panels (c) and (d) of Fig. 2 for the backgrounds with zero-wave vectors. The frequency of the backgrounds

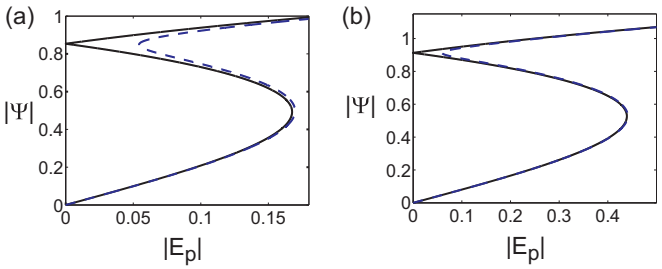

FIG. 3. (Color online) The bifurcation diagrams for the conservative case $\gamma_1 = \gamma_2 = 0$ (black solid line) and dissipative case $\gamma_1 = \gamma_2 = 0.03$ (blue dashed line) are shown in panel (a) for $\Delta_1 = \Delta_2 = 0.7$. The same pair of diagrams except that $\Delta_1 = \Delta_2 = -1.5$ are shown in panel (b).

depends on the effective detuning $\tilde{\Delta}_2$ as

$$\omega_{\pm 0} = \frac{-\Delta_1 - \tilde{\Delta}_2 \pm \sqrt{(\Delta_1 - \tilde{\Delta}_2)^2 + 4}}{2}, \tag{5}$$

where subindex 0 refers to the fact that the backgrounds have zero-wave vectors. In the expression given by Eq. (5) the + and − signs correspond to the backgrounds having the structures of the upper and the lower linear polariton modes, respectively. In the case of a background having zero frequency, the nonlinearity increases the effective detuning $\tilde{\Delta}_2$, which is indicated by the right arrows in Fig. 2. From panels (c) and (d) of Fig. 2 one can see that the discussed background can exist only if the linear detuning Δ_2 is lower than a certain critical value Δ_{20}. The intervals of linear detuning Δ_2, where there may exist the background having zero frequency are indicated by thick blue and black horizontal lines in panels (c) and (d).

Now we show that for the positive and negative Δ_1 the background has a structure of the upper or the lower polariton modes, respectively. The equality $\omega_{\pm 0} = 0$ yields $(\Delta_1 + \tilde{\Delta}_{20})^2 = (\Delta_1 - \tilde{\Delta}_{20})^2 + 4$ ($\omega_{\pm 0} = 0$ at $\tilde{\Delta}_{20}$), which is equivalent to $\tilde{\Delta}_{20} = 1/\Delta_1$. Let us assume that Δ_1 is positive; then $\tilde{\Delta}_{20}$ is positive too. Therefore, the term $-(\Delta_1 + \tilde{\Delta}_{20})$ is negative and it can be compensated only when the square root in (5) is taken with the + sign. It means that for positive Δ_1 only the upper mode can be tuned into the resonance. The nonlinear effects increase the effective $\tilde{\Delta}_2$ and we can conclude that nonlinear tuning into the resonance is possible only if $\Delta_2 < \tilde{\Delta}_{20} = 1/\Delta_1$; see Fig. 2(c). A completely analogous analysis that can be carried out in the case of negative Δ_2, reveals that the lower mode can be tuned in the resonance provided the condition $\Delta_1 < 0$, $\Delta_2 < 1/\Delta_1$ is satisfied; see Fig. 2(d).

By introducing a finite pump the symmetry becomes broken and a pair of backgrounds bifurcate from the zero-pump background. One of these backgrounds is stable and another is unstable. It is obvious that the background bifurcating from the trivial solution is always stable. The bifurcation diagrams which show the dependencies of the amplitude of $|\Psi|$ field on the pump E_p are shown in Fig. 3. The analysis outlined above can also be carried out for the dissipative case, although the algebra becomes more complicated and is less instructive from the physical point of view. In Fig. 4 we display the areas in the

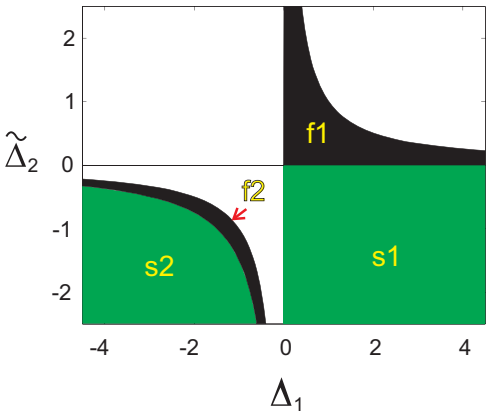

FIG. 4. (Color online) The regions of parameters on parameter plane Δ_1-$\tilde{\Delta}_2$, where there is an intrinsic bistability and the spatially uniform background has the structure of the upper branch (f1,s1) and lower branch (f2,s2). All equilibrium states describing spatially uniform states belong either to the same phase plane (f1 and f2) or different phase planes (s1 and s2).

parameter plane $\Delta_1 - \tilde{\Delta}_2$, where the bistability of spatially uniform states exist for the conservative case. Specifically, we determined the regions in the parameter plane $\Delta_1 - \tilde{\Delta}_2$, where the upper (f1,s1) and lower (f2,s2) branches can be tuned into the resonance, where the indices 1,2 refer to the cases when the states belong to the same and the different phase plane, respectively.

IV. CONSERVATIVE SOLITONS

The stationary fields are governed by the system of ordinary differential equations

$$\partial_x^2 E + (i\gamma_1 + \Delta_1)E + \psi = E_p, \tag{6}$$

$$\sigma \partial_x^2 \psi + (i\gamma_2 + \Delta_2 + |\psi|^2)\psi + E = 0. \tag{7}$$

In this section we consider the 1D conservative case $\gamma_1 = \gamma_2 = 0$. This problem is relatively simple and can be treated analytically. It constitutes a good starting point for the understanding of a more complicated case of dissipative solitons. In the conservative case the solution can be found in the form of pure real functions. When we assume vanishing coefficient of the diffraction of the resonators mode to be $\sigma = 0$, the dimensionality of the phase space of the ordinary differential equations describing the stationary solutions is significantly reduced. The equations for stationary solutions read

$$\partial_x^2 E + \Delta_1 E + \psi = E_p, \tag{8}$$

$$(\Delta_2 + \psi^2)\psi + E = 0. \tag{9}$$

A crucial point here stems from the fact that the second equation is an algebraic one and the phase space of the whole system is only 2D. Now let us consider the phase plane of Eq. (9). By using the second equation one can express the amplitude of the resonator mode ψ as a function of the cavity

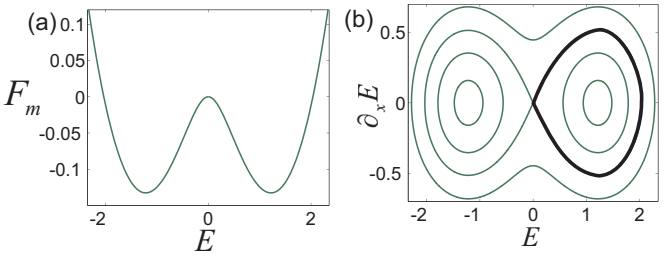

FIG. 5. (Color online) (a) Potential $F_m(E)$ and (b) the phase plane, where the homoclinic trajectory corresponding to a soliton is indicated by a thicker line. The parameters are $\Delta_1 = \Delta_2 = 0.7$.

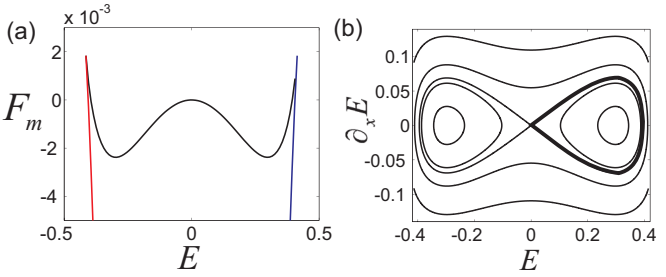

FIG. 6. (Color online) Panels (a) and (b) show the potentials and the phase plane, respectively, for the case when Eq. (9) has three real solutions $\psi = \psi_m(E)$, while the whole homoclinic trajectory of Eq. (11) belongs to only one phase plane. The parameters are $\Delta_1 = \Delta_2 = -1.05$.

field E. Then the function $\psi = \psi(E)$ can be substituted into the first equation and the set of Eqs. (8) and (9) can be reduced to the second-order nonlinear differential equation for the field E.

However, Eq. (9) can have either one or three solutions $\psi_m(E)$, where m denotes number the solutions. Each of the roots of Eq. (9) will generate a nonlinear second-order ordinary differential equation describing motion of a particle in a potential

$$F_m(E) = \frac{\Delta_1 E^2}{2} - \frac{3\psi_m^4(E)}{4} - \frac{\Delta_2 \psi_m^2(E)}{2}, \qquad (10)$$

while the equation for the field E can be expressed as

$$\partial_x^2 E + \frac{\partial F_m}{\partial E} = 0. \qquad (11)$$

When the dependence $\psi(E)$ is unique we can identify the homoclinic trajectories corresponding to soliton solutions. These solitons have one characteristic scale defined by the interplay between the diffraction of the cavity mode and the effective nonlinearity associated with the nonlinear resonators. Hereafter we refer these solitons as single-core solitons. The behavior of the single-core solitons is demonstrated in Fig. 5, where we display the potential $F_m(E)$ and the phase plane when $\Delta_1 = \Delta_2 = 0.7$. In the latter figure the trajectory corresponding to the soliton is indicated by the thicker line and the parameters of the system belong to area f1 shown in Fig. 4.

The situation is more interesting when Eq. (9) has three different roots. In this case there are three different equations and the solution can be given by any of them. We note that it is possible to switch between the solutions provided that E and $\partial_x E$ remain continuous. Each of the switches will correspond to the discontinuity in the ψ field, which is, however, not prohibited if the diffraction of the ψ field is neglected, i.e., when $\sigma = 0$. It opens a possibility to design a family of soliton solutions with discontinuities in the ψ field. Let us consider the soliton solutions in more detail. We start with the case of negative $\Delta_1 < 0$ when the soliton trajectory can comes close to the equilibrium point corresponding to the spatially uniform solution having the structure of the lower polariton mode. It yields the reason to expect that the field in such a soliton is also similar to the field in the lower polariton mode. In the absence of the pump $E_p = 0$ the trivial solution $(E = 0, \psi = 0)$ is a saddle. If $\Delta_2 < 1/\Delta_1$, then there is another steady state; in fact, there are two symmetric states $E_1 = -E_2$, $\psi_1 = -\psi_2$. A simple algebra shows that for zero pump $E_p = 0$ all steady states are given by one potential if $\frac{3}{2\Delta_1} < \Delta_2 < \frac{1}{\Delta_1}$ and the equilibrium points corresponding to the backgrounds with nonzero intensity are centers.

However, the fact that all three equilibrium points belong to the same phase plane does not necessarily mean that there are homoclinic trajectories starting and ending at the zero steady state. One can prove that for these trajectories (corresponding to bright solitons) to exist, an additional condition $\Delta_2 > \frac{9}{8\Delta_1}$ must be satisfied. Then there are two homoclinic trajectories corresponding to bright solitons. The potentials, the phase plane, and the solution are shown in Fig. 6. In the presence of the pump the situation is similar except that the symmetry of the nontrivial states is broken and there are two nonequivalent homoclinic trajectories starting and ending at the lowest state. One has to keep in mind that the latter solutions exist when the pump is within the bistability region provided that there exist three different spatially uniform solutions.

In the case when $\Delta_2 < \frac{3}{2\Delta_1}$, each of the potentials has a maximum and the steady states are all saddles belonging to different phase planes. This is illustrated in Fig. 7, where the potentials, the phase planes, and one of the possible localized solutions is shown. Let us note here that there may be an infinite number of such solutions with discontinuities because the positions and the number of the discontinuities can be chosen arbitrarily. The soliton solutions are the trajectories (that can include switches between the phase planes) starting and ending at the saddle points. In the case of the soliton solutions nestling on the lower homogeneous state, the trajectory starts and ends at the point $E = 0$, $\partial_x E = 0$ belonging to the middle phase plane; see the thicker magenta lines in Fig. 7. This trajectory can switch to another plane at some point; in our case, it switches to the upper phase plane (the continuation of the trajectory is indicated by the magenta line), then at the symmetric point the trajectory may switch back to the middle phase plane and return to the initial steady state. The E and ψ fields of the solution of such kind are shown in panels (b) and (c) of Fig. 7. It is worth noticing here that the distance between the discontinuities can be chosen arbitrarily from the range of the allowed values. We note that the width of the central area of the soliton, where the nonlinear effects are important, does not coincide with the distance between the discontinuities. Therefore, the central area of the soliton

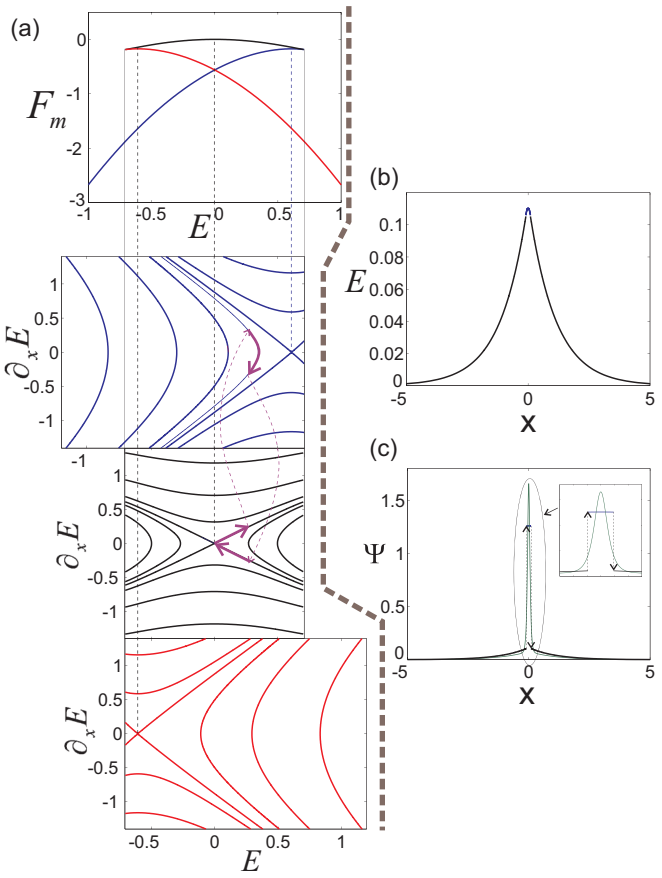

FIG. 7. (Color online) Panels (a) and (b) show potential and the phase planes, respectively; the trajectory corresponding to a soliton is indicated by a thicker line and the switchings from one phase plane to another are indicated by thinner dashed lines. Panels (b) and (c) show the solutions for the E and the ψ fields; the inset in panel (c) shows the structure on the ψ field in the core of the soliton: The thicker dark line corresponds to $\sigma = 0$ and the thinner green line shows the continuous solution for relatively small $\sigma = 0.0025$. The parameters are $\Delta_1 = \Delta_2 = -1.5$.

consists of two cores: The first one corresponds to the area where nonlinear effects define the variation of the field, while the second core corresponds to the area given by the distance between the discontinuities in the ψ field.

A. Structural and dynamical stability of conservative solitons

Now we examine whether the solutions with discontinuities in the ψ field are structurally stable, i.e., if the solution undergoes only slight modification when we introduce very small but finite diffraction in the ψ field. The structural stability is an important issue because the discontinuities in the ψ field make the term $\sigma\partial_x^2\psi$ singular. In fact, it may happen that even very weak direct interaction in the Ψ field can destroy soliton solutions and, therefore, these solutions do not have physical importance. To examine the structural stability, we study how stationary linear excitations decay to the zero background. When $\sigma \neq 0$, the dimensionality of the phase space increases from 2 to 4 and two more eigenvalues governing the relaxation of the tails to the background appear. The relaxation law is given by the expression

$$k^2 = \frac{\Delta_2 + \sigma\Delta_1 \pm \sqrt{(\Delta_2 + \sigma\Delta_1)^2 + 4(1 - \Delta_1\Delta_2)}}{2\sigma}. \quad (12)$$

For the parameter areas f2 and s2 in Fig. 4 all four roots k of Eq. (12) are pure imaginary and, therefore, the asymptotics of the stationary solutions decay to zero. This reveals that a finite σ does not generate a resonance between the soliton and the linear modes (otherwise, there may exist only so-called embedded solitons). To prove the existence of the soliton solutions for a finite σ, we compute them numerically. The numerical simulations reveal that for a finite σ the discontinuities in the ψ field transform into the steep but smooth parts of the curve. Therefore, we can claim that the solitons are structurally stable. It is worth mentioning that the finite value of σ not only smooths the discontinuities but also uniquely defines the width of the second core.

A typical solution for small σ is shown in panels (b) and (c) of Fig. 7, indicated by the thinner green line. The distribution of the E field for small σ nearly coincides with the distribution of the field E field for $\sigma = 0$, in fact, the mismatch between the curves is too small to be noticed in panel (b). In contrast, the difference in the ψ field distributions is clearly visible in the core area of the soliton.

When the upper branch can be tuned into the resonance($\Delta_1 > 0$), two of the four roots k given by Eq. (12) are pure imaginary, while other two are pure real. Indeed, in this case the region of the bistability of the spatially uniform states is given by the condition $\Delta_2 < 1/\Delta_1$. Then for the positive Δ_2, which corresponds to the region f1 (Fig. 4), we obtain the condition $0 < 1 - \Delta_1\Delta_2$ and, therefore, the square root in Eq. (12) is always larger than the absolute value of $\Delta_2 + \sigma\Delta_1$. It is obvious that the condition $0 < 1 - \Delta_1\Delta_2$ is satisfied also in the region s1 because in the latter the conditions $\Delta_1 > 0$ and $\Delta_2 < 0$ apply. As a result, one pair of the wave vectors k is always imaginary, while the other pair is always real in these parameter regions. It means that in the general case the soliton tails do not decay to zero if the soliton parameters belong to the regions f1 or s1.

To understand the statement from the physical point of view, let us look at the dispersion relation for the linear waves propagating in the system characterized by the parameters from the f1 or s1 regions. For $\sigma \neq 0$ the gap between the two branches is closed, which means that the solitons existing in this gap for $\sigma = 0$ in general disappear for finite values of σ because they are in resonance with linear waves. Therefore, for positive Δ_2 only embedded solitons can exist.

We note that in the presence of dissipation the tails of stationary solutions do decay to the spatially uniform state and therefore the dissipative solitons nestling on the upper branch can be found. However, one might anticipate that they are weakly localized for small losses. In this paper we focus on the solitons existing in the areas s2 and f2 while the solitons nestling on the upper polariton branch are left for future research.

Let us discuss the properties of the solitons in the areas f2 and s2. The soliton fields in the region f2 are wide and not intensive in the vicinity of the border of the domain of the soliton existence. When the values of Δ_1 and Δ_2 come close to the boundary between areas f2 and s2, the intensities of the

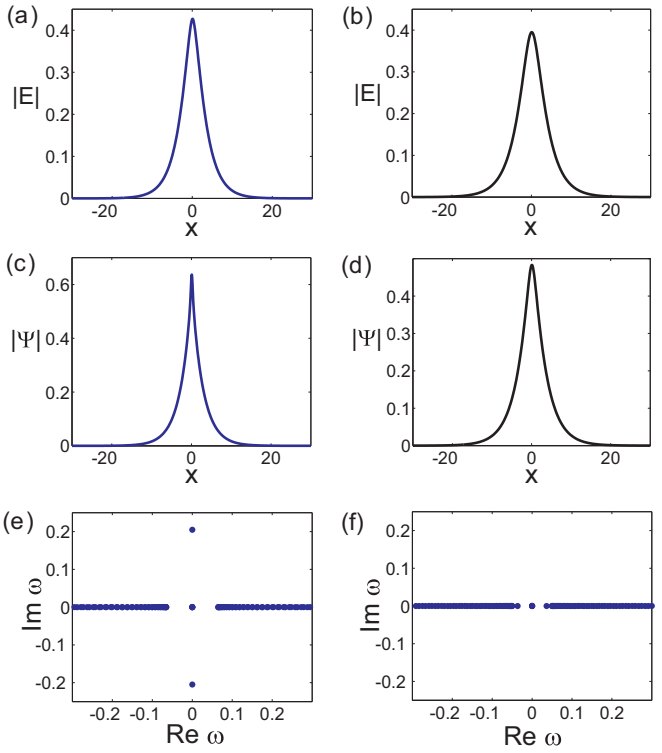

FIG. 8. (Color online) The distributions of the E and ψ fields for the conservative solitons in the region f2 are shown for $\Delta_1 = \Delta_2 = -1.065$ [panels (a) and (c)] and for $\Delta_1 = \Delta_2 = -1.05$ [panels (b) and (d)]. The spectra governing the stability of the solitons are shown in panels (e) and (f). The pump E_p is equal to zero for both cases, the diffraction in the ψ field is $\sigma = 0.0025$.

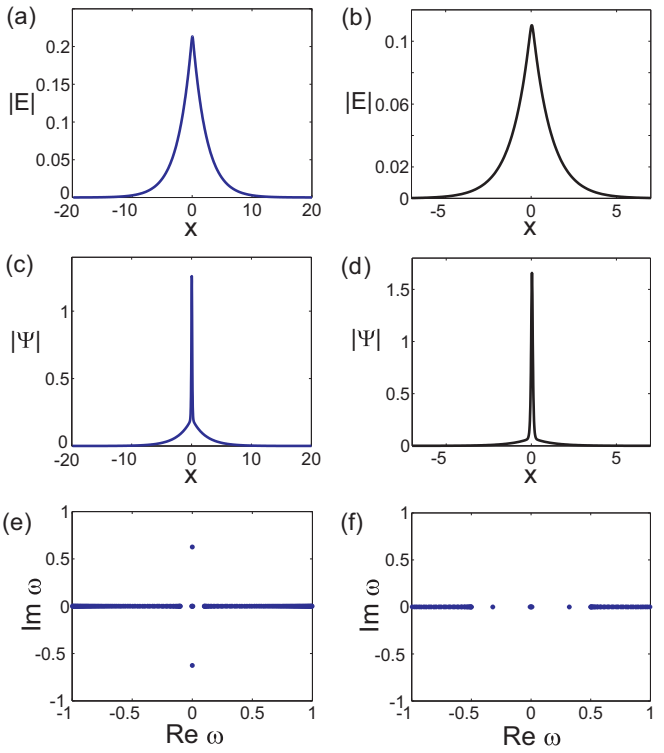

FIG. 9. (Color online) The distributions of the E and ψ fields for the conservative solitons in the s2 region are shown for $\Delta_1 = \Delta_2 = -1.1$ [panels (a) and (c)] and for $\Delta_1 = \Delta_2 = -1.5$ [panels (b) and (d)]. The spectra governing the stability of the solitons are shown in panels (e) and (f). The pump is equal to zero for both cases; the diffraction in the ψ field is $\sigma = 0.0025$.

soliton fields increase; see panels (a) and (b) in Fig. 8, where distributions of the E fields are shown for $\Delta_1 = \Delta_2 = -1.065$ and $\Delta_1 = \Delta_2 = -1.05$. Panels (c) and (d) display the ψ-field distributions for the same parameters.

When the values of Δ_1-Δ_2 enter s2 region, a narrow second core develops in the resonators field ψ in the center of the soliton. For the values of Δ_1 and Δ_2 belonging to the area s2 of Fig. 4 one can observe the formation of a dual core soliton with two different characteristic scales. This feature is more clearly seen in the distribution of the resonators field ψ; however, it is also visible for the cavity field E.

Let us remind the reader that for $\sigma = 0$ there are discontinuities in the ψ field and a pair of these discontinuities transforms into a narrow second core of the soliton for finite σ. However, E and $\partial_x E$ are continuous for $\sigma = 0$; the discontinuity occurs only in $\partial_x^2 E$. The discontinuity in the second spatial derivative of the E field manifests itself in a very abrupt change in the spatial dependence of the E field in the center of the soliton. The characteristic size of this sharp feature is equal to the characteristic width of the narrow pattern in the ψ field.

Finally, we remark that it is not correct to consider the discussed dual-scale solitons as a solitary structure with the wings having different decay rates. It is important to point out that the highly nonlinear central region of the soliton has two different characteristic scales.

From a physical point of view the dynamical stability of the solitons is of fundamental importance because only stable solitons can be observed in experiments. We studied the dynamical stability of the solitons by solving the spectral problem for the weak excitations on the background of the soliton. The spectra obtained for the conservative case are shown in panels (e) and (f) in Figs. 8 and 9. One can see that in the region f2 the (single-core) solitons with relatively low Ψ field intensity are stable; see panel (f) in Fig. 8, which shows the eigenfrequencies of the linear excitations. When the soliton intensity increases, two discrete eigenvalues within the gap collide in the center and produce two pure imaginary frequencies governing the growth rate of the unstable mode; see panel (e) in Fig. 8. In the region s2 the situation is the opposite. The dual-core solitons with relatively low Ψ-field intensity are unstable [panel (e) of Fig. 9], while for higher intensity and a more pronounced second core the solitons become stabilized [panel (f) in Fig. 9]. We inspected the stability by direct numerical simulation of the master equations (2) and (3) by imposing the initial conditions in the form of the soliton solution perturbed by a weak noise. The results of the direct numerical simulations are shown in Fig. 10. One can see that initially the soliton propagates without any strong perturbations and then the instability gradually sets in and destroys the soliton, which splits into two dispersive wave envelopes.

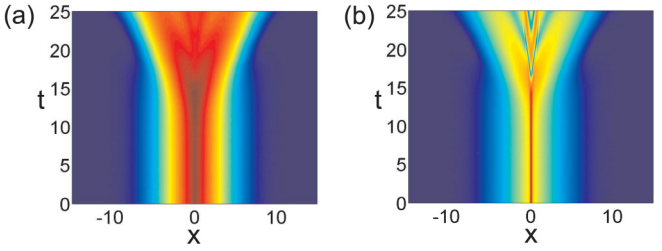

FIG. 10. (Color online) The temporal evolutions of the intensities of the field $\mathcal{E}$ (a) and field Ψ (b). A soliton solution corresponding to $\Delta_1 = \Delta_2 = -1.1$ perturbed by weak noise was taken as the initial condition. The pump E_p is equal to zero, the diffraction in the Ψ field is $\sigma = 0.0025$.

B. Adiabatic decay of the dual-core solitons

In this section we consider the adiabatic evolution and a decay of the solitons caused by small losses in the absence of the pump. We assume the initial condition in the form of a conservative dual-core soliton and we study its dynamics in the presence of weak losses.

Initially, the dual-core soliton is intense and therefore stable (the soliton belongs to the region s2). In the presence of small losses the soliton intensity slowly decreases due to the dissipation, while the distributions of the fields remain to resemble those of the conservative soliton. To fit the time-dependent fields by the soliton, its parameters must vary in time. Namely, $\Delta_{1,2}$ are decreasing functions of time $\Delta_{1,2} = \overline{\Delta}_{1,2} - Q(t)$, where $\overline{\Delta}_{1,2}$ are the initial values of $\Delta_{1,2}$ and $Q(t)$ is a positive monotonically increasing function accounting for the adiabatic variation of the soliton frequency.

The fact that low-intensity dual-core solitons are dynamically unstable allows us to anticipate that at some moment the intensity of a slowly decaying soliton will reach the threshold value when the instability sets in. Beyond this threshold the soliton is assumed to decay rapidly into dispersive waves due to the instability. To verify this hypothesis we performed numerical simulations of the dynamics of the soliton. The typical results are shown in panels (a), (c) and (b), (d) in Fig. 11, which display the evolution of the quasisoliton fields for several values of the dissipation. We emphasize the resemblance of the quasisoliton evolutions in the stage of a rapid decay to those belonging the unstable conservative soliton shown in panels (a) and (b) in Fig. 10.

Alternatively, we also imposed the initial condition such that the initial Ψ field is chosen to be in the form of the conservative soliton field distribution multiplied by the factor 1.1 and zero initial field $\mathcal{E}$. The typical evolutions of the fields are shown in panels (e) and (f) in Fig. 11. In this case, we observe the formation of a strongly localized oscillatory state instead of the soliton. We assume that the formation of the oscillating structure occurs due to the excitation of the internal mode of the soliton (there is a pair of discrete nonzero eigenvalues in the gap of the soliton spectrum). The energy of the localized structure decreases with time but the field remains localized until the intensity of the soliton reaches the threshold value and the soliton rapidly collapses beyond the threshold.

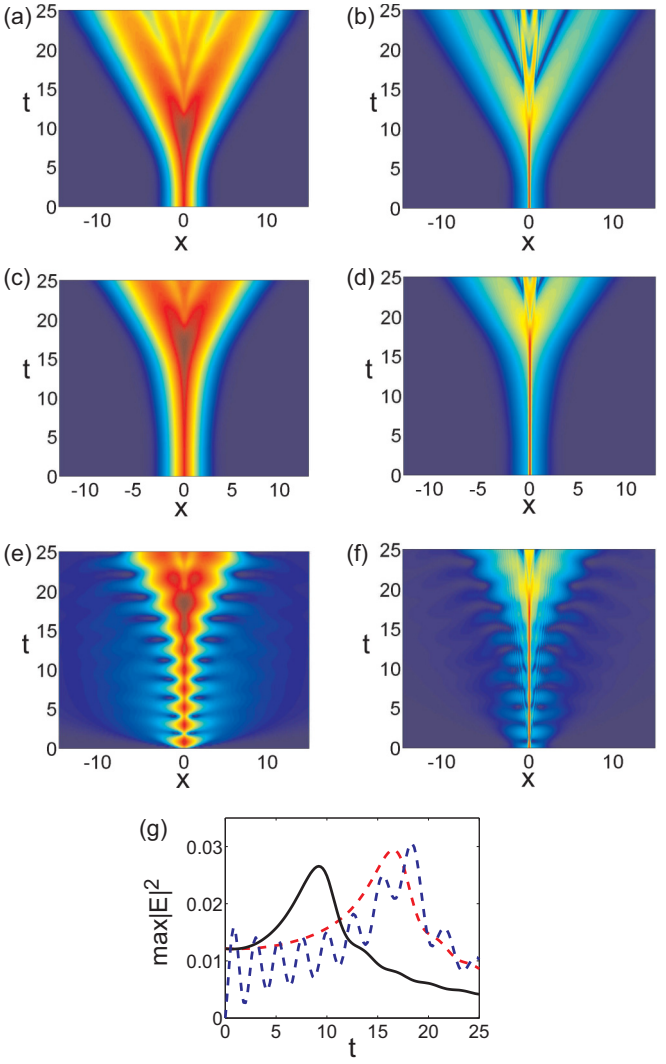

FIG. 11. (Color online) Panels (a) and (b) show the temporal evolution of the $\mathcal{E}$ and Ψ fields, respectively, in the system with the dissipation $\gamma_1 = \gamma_2 = 0.005$. A conservative soliton calculated for initial conditions $\overline{\Delta}_{1,2} = -1.5$. The same but for $\gamma_1 = 0.005$ and $\gamma_2 = 0.0005$ is shown in panels (c) and (d). Panels (e) and (f) show the evolution for the case $\gamma_1 = \gamma_2 = 0.005$ when the initial conditions are assumed in the form of the conservative soliton field distribution multiplied by factor 1.1 for the Ψ field and zero initial conditions for the field E. Panel (g) displays the evolution of the maximum absolute value of the E field for the first (black solid line), second (red dashed line), and the third (blue dashed line) cases. The pump is equal to zero for all cases; the diffraction in the Ψ field is $\sigma = 0.0025$.

It is interesting to note that the decrease of the energy of the dual-core soliton leads to the increase of the maximal intensity of the $\mathcal{E}$ field. It means that the dual-core cavity soliton of lower energy looks brighter for the observer because only the cavity mode shines out from the cavity. It is illustrated in panel (g) in Fig. 11 where the dependencies of the maximum intensity of $\mathcal{E}$ field vs time are shown. One can see that the brightness of the soliton increases and reaches maximum approximately at the moment when the soliton starts to decay.

V. STRUCTURAL STABILITY AND DYNAMICS OF THE DISSIPATIVE SOLITONS

The existence of stationary solitons in the dissipative systems requires the presence of a pump. In this section we consider stationary dissipative cavity solitons with the resonant pump. In the dissipative case, the phase space is 4D for $\sigma = 0$ and 8D when σ is nonzero. This renders a complete analytical description rather difficult even in the simplest case $\sigma = 0$; however, the mechanism of the formation of dual-core solitons persists. In the case $\sigma = 0$ Eq. (7) transforms into an algebraic equation,

$$(i\gamma_2 + \Delta_2 + |\psi|^2)\psi + E = 0. \tag{13}$$

It can easily be established that the intrinsic bistability exists when $\Delta_2 < -\sqrt{3}\gamma_2$ and the lowest root of the Eq. (13) lies in the interval $0 < |\psi| < \sqrt{I_-}$, the intermediate one in $\sqrt{I_-} < |\psi| < \sqrt{I_+}$, and the upper root in the interval $\sqrt{I_+} < |\psi|$, where

$$I_\pm = \frac{-2\Delta_2 \pm \sqrt{\Delta_2^2 - 3\gamma_2^2}}{3}. \tag{14}$$

The intrinsic bistability exists for the field E lying in the interval $|E_-| < |E| < |E_+|$, where

$$|E_\pm|^2 = \left[\gamma_2^2 + \left(\Delta_2 + I_\pm\right)^2\right] I_\pm.$$

Likewise in the conservative case, the field ψ must not be continuous. Indeed, we found the dissipative solitons with the discontinuities for the parameters supporting an intrinsic bistability. We also have shown that these solutions can be dynamically stable.

In the dissipative case the issue of structural stability is also of primary importance. We found out that finite σ smooths the discontinuity but the soliton solutions survive, transforming into the solitons with two characteristic sizes: The first one is defined by the diffraction of the cavity mode while the second one corresponds to the healing length of the discontinuity governed mostly by the strength of the interaction between resonators σ. However, in the dissipative case the soliton intensity depends not only on the soliton frequency (which is equal to the frequency of the pump) but also on the intensity of the pump. It means that for some parts of the bifurcation curve the cavity soliton possesses a single-scale core while for the other parts of the same bifurcation curve the core of the soliton has two characteristic scales. The bifurcation diagrams for different detunings are shown in Fig. 12. Let us denote a critical value of the ψ field as $|\psi_{th}| = \sqrt{I_-}$ such that all $|\psi| > |\psi_{th}|$ are given by the intermediate or the largest root of the Eq. (7). The soliton trajectory starts on the lowest background [which is given by the lowest root of the Eq. (13)] and goes around another fixed point. For certain parameters it happens that the maximum amplitude of the soliton field exceeds ψ_{th}. Then at this point the soliton trajectory must switch to a trajectory belonging to the phase space generated by another root $\psi(E)$. Indeed, our numerical simulations indicate that when ψ passes the critical value, a folding point appears on the bifurcation characteristics. At the same time a narrow pattern starts to develop in the core of the soliton. Hereafter we refer this folding point as an intrinsic bistability folding point (IBFP). It is important to note here that for small σ the

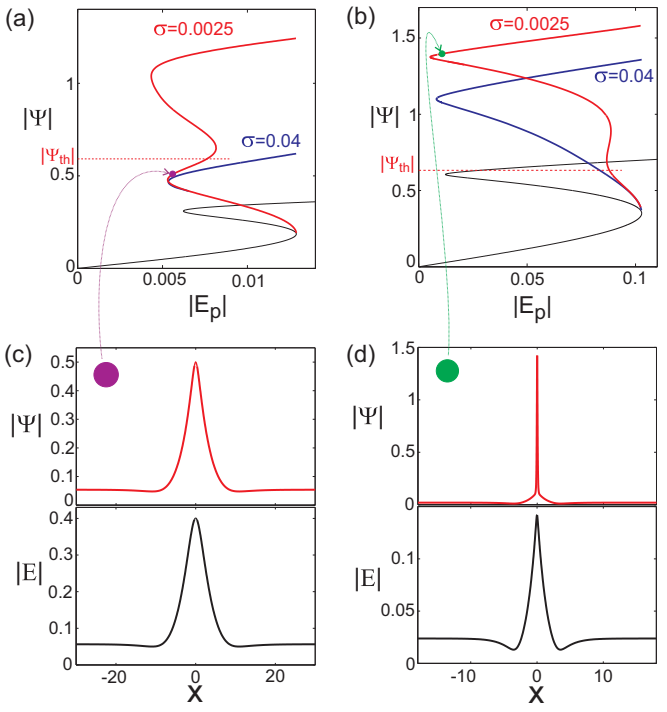

FIG. 12. (Color online) The bifurcation diagrams for dissipative solitons showing the dependencies of the maximum absolute value of the ψ field of the soliton on the pump field E_p. The red and blue lines correspond to $\sigma = 0.0025$ and $\sigma = 0.04$, respectively. The dashed red lines indicate the threshold values ψ_{th}. Panel (a) illustrates the case $\Delta_2 = \Delta_1 = -1.05$ when the threshold value $|\psi_{th}|$ lies above the FFP of the soliton bifurcation curve. The case $\Delta_2 = \Delta_1 = -1.2$ is shown in panel (b), the threshold value $|\psi_{th}|$ lies below the FFP of the soliton bifurcation curve. The black curves in panels (a) and (b) show the bifurcation diagrams for the spatially uniform states. The field distributions of the single- and dual-core solitons are shown in panels (c) and (d) for $\Delta_2 = \Delta_1 = -1.05$ and $\Delta_2 = \Delta_1 = -1.2$, respectively; the diffraction in the ψ field $\sigma = 0.0025$. The soliton solutions shown in panels (c) and (d) correspond to the points on bifurcation diagrams (a) and (b) indicated by the purple and the green circles. The losses are $\gamma_1 = \gamma_2 = 0.01$.

folding point appears close but not exactly at the threshold point found for $\sigma = 0$; see panels (a) and (b) in Fig. 12. The typical distribution of the fields in the dissipative single- and dual-core solitons are shown in Fig. 12(d) for a small value σ. For larger σ the IBFP becomes less sharp and disappears for a sufficiently large value of σ; see the bifurcation curves for $\sigma = 0.0025$ and $\sigma = 0.04$ in Fig. 12. Then the bifurcation diagram of the soliton has only one folding point, which we refer to as a fundamental folding point (FFP).

Now we address a dynamical stability of dissipative solitons. We have studied the stability by solving the corresponding spectral problem numerically and by direct numerical simulation of the master equation. The stability properties of the dissipative solitons are very rich and require special consideration which is out of the scope of the present paper. However, it is important to point out that the dissipative dual-core solitons can be stable and thus amenable to experimental verification.

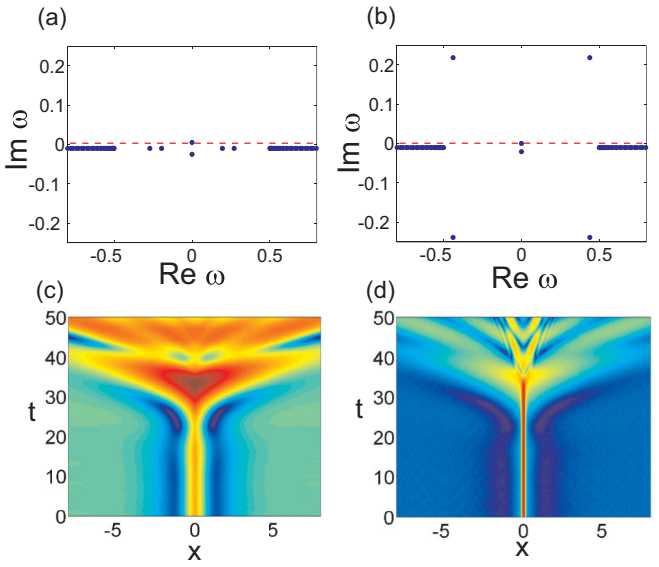

FIG. 13. (Color online) The eigenfrequencies for the stable (a) and unstable (b) dual-core dissipative solitons. The pumps are $E_p = 0.0106$ for the stable soliton and $E_p = 0.085$ for its unstable counterpart. The eigenvalues above the red dashed line $\mathrm{Im}\omega = 0$ correspond to the unstable modes. The development of the instability is illustrated in panels (c) and (d), showing the temporal evolutions of the $\mathcal{E}$ and Ψ fields, respectively. The other parameters are $\Delta_2 = \Delta_1 = -1.5$, $\gamma_1 = \gamma_2 = 0.01$.

Based on the results of our numerical simulations, we found that the stable soliton usually belongs to the upper branch of the bifurcation curve close to the folding point. The increase of the pump and, correspondingly, the intensity of the soliton result in the instability of the soliton. In panel (a) in Fig. 13 we present the spectrum of a stable dual-core soliton. The spectrum reveals one zero eigenvalue corresponding to the translational symmetry of the soliton. Besides this translational mode, the other excitations are characterized by the frequencies with negative imaginary parts which predict the soliton to be stable. The stability has been confirmed by direct numerical simulation when the initial conditions were assumed to be in the form of a soliton perturbed by weak noise.

The discrete part of the spectrum shown in Fig. 13 has six eigenvalues. When the pump increases two pairs of them collide and then the imaginary values of two of the eigenvalues crosses the horizontal axes and become positive and give rise to the instability. The spectrum of the unstable soliton is shown in panel (b) in Fig. 13. The onset of the instability is illustrated in panels (c) and (d) showing temporal evolution of the $\mathcal{E}$ and Ψ fields. One can see that the instability leads to the collapse of the soliton.

We conclude the section with the following two notes. First, the instability discussed above is not the only one that can exist in the considered system. We have chosen it as an example because this kind of instability is typical at the boundary separating stable and unstable dual-core solitons. Second, we have demonstrated the existence of the single-core dissipative solitons nestling on the lower branch of the dispersion relation; however, we have not found any significantly new features associated with these solitons. Since our paper is primarily devoted to the dual-core solitons, we omit the discussion of the single-core dissipative solitons. Likewise, we do not discuss the solitons nestling on the upper branch of the dispersion characteristics although, in general, they can exist in contrast to the conservative case. These issues will be addressed elsewhere.

VI. DISCUSSION AND CONCLUSION

We studied theoretically and numerically the formation and dynamics of the solitons in the cavities with built-in nonlinear resonators represented by the metallic nanoparticles embedded in a planar FP cavity filled with a nonlinear medium. The dispersion in the system is mainly supplied by the cavity mode, whereas the nonlinearity is provided by the resonators.

To estimate the realistic parameters of the envisaged resonator which makes it possible to investigate the dynamics of the dissipative solitons, we have used an effective medium approach which describes the cavity in terms of the effective dielectric function. We have found that the effective damping associated with losses in the Au or Ag nanoparticles does not allow achieving of sufficiently large Q factor of the resonator which may support the formation of the dissipative solitons. To overcome this limitation, we suggest replacing lossy nanoparticles with active coated ones, which leads to significant reduction of the width of the extinction coefficient that characterizes the localized plasmon resonance associated with such nanoparticles. We have demonstrated, using the example of Ag-coated nanoparticles, that for sufficiently high pump power the active material compensates for the losses and one can achieve sufficiently large enhancement of the surface plasmon field in the vicinity of the nanoparticle that would consequently allow achieving a sufficiently large Q factor of the resonator.

Then we studied the soliton solutions of the mathematical model consisting of two coupled equations for the amplitudes of the cavity mode and the resonators mode. It was shown that in the case of the focusing nonlinearity there may exist solitons nestling on the mode belonging to the lower branch of the dispersion characteristics. It is important to point out that the core of the solitons can have two different scales in the case when the built-in resonators do not interact with each other directly, i.e., the diffraction of the resonators field is small $\sigma \approx 0$.

For vanishing diffraction of the resonator field $\sigma = 0$, we studied analytically the conservative solitons with discontinuities in the resonators field. It was shown numerically that these solitons with discontinuities are structurally stable and that small diffraction in the resonators field smooths the discontinuities but does not destroy the solutions. To investigate the dynamical stability of the solitons, we solved numerically the spectral problem governing the stability of the solitons. We found that the dual-core solitons can be dynamically stable and thus they can be observed experimentally. To confirm the results of the spectral analysis and to study the development of the instability, we performed direct numerical simulations of the dynamical equations. We found that unstable solitons collapse. Further, we studied numerically the behavior of quasisolitons in the presence of weak losses. It was shown that the losses result in the adiabatic variation of the soliton

parameters until the quasisoliton reaches the intensity at which the soliton collapses.

We also investigated the properties of the dissipative solitons in the presence of the pump; we found the field distributions in the solitons and calculated their bifurcation curves. It was shown that for a weak diffraction of the ψ field the intrinsic bistability gives rise to a folding point on the bifurcation diagram. The stability of the dissipative solitons were studied by solving the spectral problem for small excitations on the soliton solutions and by direct numerical simulations of the dynamical equations. It was established that the dissipative solitons can be stable and thus offer a possibility of experimental observation. The typical scenarios of an instability onset were considered and demonstrated by numerical simulations.

The main goal of the paper was to explore the properties of the dual-core solitons nestling on the lower branch of the dispersion characteristics, however, we would like to acknowledge that the systematic study of the solitons nestling on the upper branch, the problem of the soliton motion and the related issues are of much interest as well and they will be addressed elsewhere.

The dual-scale solitons can be seen as an optical analogy of such objects as Abrikosov vortices in superconductors that also have two characteristic scales. In superconductivity the equation for the magnetic field is linear and possesses a large characteristic scale. In contrast, the equation for the order parameter is nonlinear and is characterized by a very short spatial characteristic scale. In this sense the resonators mode in the optical system considered here is analogous to the order parameter in superconducting systems and the cavity field in the optical system is analogous to the magnetic field in the superconducting counterpart. These properties link our optical system to the superconductors of the second kind. One has to keep in mind however, that the mechanisms of the interactions between the subsystems are profoundly different.

Finally, we note that the existence of a very narrow core of the solitons can prove to be of great importance for practical applications. For example, the narrow core should make the soliton very sensitive to the spatial inhomogeneities of the cavity and therefore the dual-core soliton controlled by the holding beam can be used for the scanning the cavities and in the measuring of their local characteristics.

ACKNOWLEDGMENTS

A.V.Y. acknowledges support of the Government of the Russian Federation (Grant No. 074-U01) through ITMO Early Career Fellowship scheme. V. K. acknowledges support of the Grant No. LD14028 of Czech Ministry of Education within COST Action MP1204.

APPENDIX

To perform numerical 3D simulations of our system we used OPTIFDTD software [36], which employs the FDTD approach [37] that produces a direct numerical solution of the time-dependent Maxwell's curl equations. To get a spectral response FDTD as a time-domain simulation method, a discretized Fourier transform is used. The calculated transmitted power

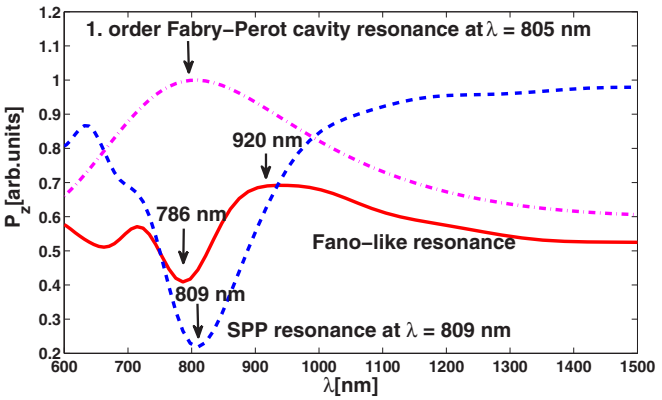

FIG. 14. (Color online) The transmitted power as a function of wavelength in the FP cavity with Au nanoparticles calculated by the FDTD method: the localized SPP resonance associated with a Au nanoparticle in SiO_2 without a FP cavity (blue dashed line); the lowest FP resonance at $\lambda = 805$ nm (magenta dash-dotted line); Fano-like resonance associated with a Au nanoparticle in the FP cavity (solid red line).

P_z as a function of the wavelength λ in the direction of the z axis can be calculated as a sum of two terms associated with TE and TM polarizations $P_z = P^{\mathrm{TE}}_{z-x} + P^{\mathrm{TM}}_{z-y}$, where $P^{\mathrm{TE}}_{z-x} = \frac{1}{2}\mathrm{Re}[\int\int E_x H_y^* dxdy]$ and $P^{\mathrm{TM}}_{z-y} = -\frac{1}{2}\mathrm{Re}[\int\int E_y H_x^* dxdy]$. We used a Gaussian modulated continuous-wave propagating in the direction of the z axis as an input wave signal. The width of the FP cavity $L = L_1 + L_2$ (see Fig. 1) is chosen in such a way that the corresponding waveguide cutoff frequency, i.e., the lowest frequency mode supported in the FP cavity, coincides with the frequency of the surface plasmon resonance localized on the metallic nanoparticle. Namely, we consider a Au nanoparticle embedded in the silica glass in absence of a FP cavity characterized by the dielectric function $\epsilon_m = 2.1$. In Fig. 14 we present the results obtained by using the FDTD method: the transmitted power P_z vs wavelength λ for FP cavity with metallic nanoparticles. Specifically, transmitted power associated with an isolated nanoparticle placed in the silica glass without a FP cavity is indicated by the blue dashed line in Fig. 14, which reveals strong resonance associated with excitation of the localized surface plasmon mode at $\lambda = 809$ nm.

The lowest FP cavity resonance without nanoparticles occurs at $\lambda = 805$ nm (magenta dash-dotted line) when the width of the FP cavity is $d = 190$ nm. The interaction between the two modes leads to a strong modified resonance shape of the resulting transmittance, which reveals a Fano-like resonance behavior; see the red solid line possessing a peak at $\lambda = 920$ nm and a dip at $\lambda = 786$ nm corresponding to a single plasmon extinction peak. Such a behavior indicates the formation of the plasmon-polariton polariton, where a peak and a dip in transmittance indicate excitation of the lower and upper plasmon-polariton branches at normal incidence.

We note that the field pattern belonging to the mode at $\lambda = 786$ nm has strongly localized character which resembles a localized surface plasmon mode, while the distribution of the field corresponding to the mode at $\lambda = 920$ nm corresponding

to the lower plasmon-polariton branch reveals a waveguide-like-mode standing-wave pattern.

The Fano-like resonance with minimum centered at = 786 nm (blue line in Fig. 14) can be described in terms of a simple analytical model presented in [38]. In general, the microscopic origin of the Fano resonance arises from the constructive and destructive interference of a narrow discrete resonance with a broad spectral line or continuum. This phenomenon has been observed in various plasmonic nanostructures [39]. The excitations are achieved through the interference of a plasmon resonance, which acts as the continuum state (CS), with a discrete state (DS), which can be the excitation of the diffraction channel such as, e.g., gratings or plasmonic crystals or the excitation of a guided mode.

In our case we consider the interaction of a plasmonic resonance (acting as the CS) with a discrete resonance (corresponding to the lowest FP resonance), giving rise to Fano-like shape. The shape of the resonance resulting from the coupling of a SPP resonance with a FP waveguide mode has the form

$$\sigma(\mathcal{E}) = \frac{(\mathcal{E}+q)^2}{\mathcal{E}^2+1}, \tag{A1}$$

where q is the shape parameter which determines the asymmetry of the profile and $\mathcal{E} = 2(E - E_d)/\Gamma_d$ is the reduced energy, which depends on the energy of the incident photon E, the energy of the DS E_d, and its width Γ_d. The presence of the plasmonic resonance in the Eq. (A1) can be included via coupling of the DS (LSP) to the continuum that is given by $\nu\sqrt{\mathcal{L}(E)}$, where ν is the coupling factor between the CS and the DS and $\mathcal{L}(E)$ is the plasmonic line shape

$$\mathcal{L}(E) = \frac{1}{1+\left(\frac{E-E_p}{\Gamma_p/2}\right)^2}, \tag{A2}$$

with E_p and Γ_p denoting energy and width of the plasmon resonance, respectively. On the other hand, coupling of an incident photon to CS is given by $g\sqrt{\mathcal{L}(E)}$, where g is a coupling factor. From comparison between the results for the extinction coefficient obtained from FDTD numerical calculation shown in Fig. 14 we found that the width of the plasmonic resonance $\Gamma_p = 150$ nm and FP resonance $\Gamma_d = 500$ nm; see Fig. 15. The coupling of the DS to the continuum is given with a good approximation via Fermi's golden rule by $\nu^2 = \Gamma_d/2\pi$, which yields factor $\nu = 8.9$. The coupling factor g is given by the probability of exciting the plasmon resonance with a plane wave, in other words by the plasmon resonance width, that is, $g^2 = \Gamma_p/2\pi$ which for $\Gamma_p = 150$ nm yields $g = 4.9$.

We found that when the parameters Γ_p and ν that characterize plasmonic resonance shown in Fig. 14 are substituted into the homogenization model, the resulting width of the resonance associated with the cavity does not make it possible to achieve a sufficiently large value of the resonator Q factor estimated from the homogenization model to be $Q > 50$, which is required to support the existence of the dissipative solitons. In order to increase the value of the Q factor it is necessary to significantly reduce the width of the extinction coefficient associated with the plasmon resonance. This is, however, not possible to achieve by using an arbitrary lossy metallic nanoparticle because its extinction cross section is dominated by absorption.

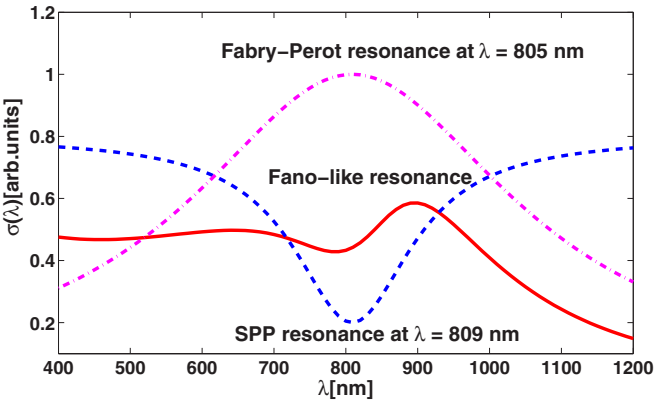

FIG. 15. (Color online) The shapes of the FP resonance at $\lambda =$ 805 nm (dash-dotted magenta line), SPP resonance at $\lambda =$ 809 nm (dashed blue line), and Fano resonance (solid red line) determined according to analytical model [38], all of which correspond to curves obtained from numerical simulations shown in Fig. 14.

On the other hand, it is well known that the optical properties of the nano-sized plasmonic particles can be significantly affected when the material absorption is compensated for. Specifically, we follow the concept of an active coated nanoparticle proposed in Ref. [40], in which it was shown that in the case of a concentric nanometer-sized spherical shell consisting of an active three-level gain medium core fabricated from rare-earth-doped silica and a surrounding plasmonic metal shell, the active material can compensate for the intrinsic losses and even overcome them so that the resulting extinction cross section is dominated entirely by radiated power. To characterize gain medium we have used a general permittivity model described in terms of the real part of the refractive index n and imaginary part of the refractive index k, which represents the optical loss or gain constant, while the permittivity is

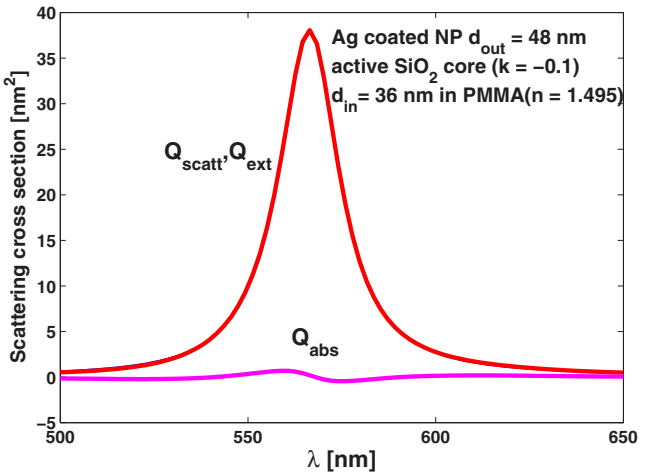

FIG. 16. (Color online) The effective scattering, extinction and absorption cross sections Q_{scatt}, Q_{ext} (red solid line), and Q_{abs} (magenta solid line) for a Ag nanoparticle embedded in PMMA with active SiO_2 core characterized with the optical gain constant $k = -0.1$.

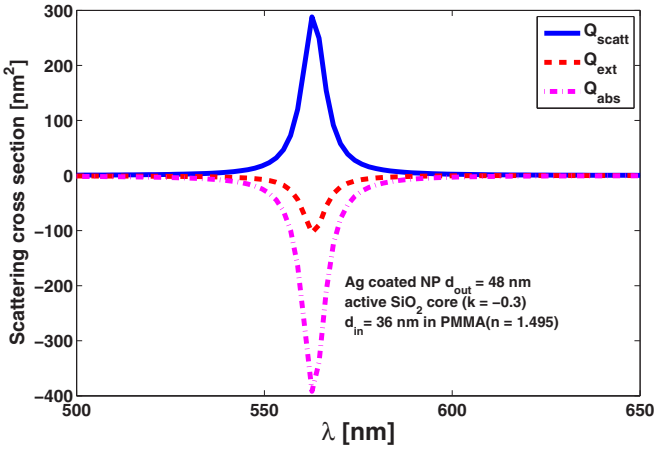

FIG. 17. (Color online) The effective scattering, extinction, and absorption cross sections Q_{scatt}, Q_{ext}, and Q_{abs} for a Ag nanoparticle embedded in PMMA with active SiO_2 core characterized with the optical gain constant $k = -0.3$.

defined as $\epsilon = n^2 - k^2 + i2kn$. By following Ref. [41] we have introduced gain by considering a susceptibility model suitable for representing such a three-level system. We used the real and imaginary parts of the rare-earth-ion-doped silica susceptibility that have been determined with the parameters $N\sigma_{em}$ and $N\sigma_{\text{abs}}$, where N is the concentration of the rare-earth ions and σ_{em} and σ_{abs} denote the emission and absorption cross section, respectively.

According to a generalized version of the Mie theory, the standard definition a positive value of the absorption cross section σ_{abs} indicates power lost due to absorption within the nanoparticle, while a negative absorption cross section is interpreted as the net power leaving the nanoparticle, i.e., the power being radiated by the active coated nanoparticle. When σ_{abs} becomes zero, the losses associated with the lossy coated nanoparticle are compensated for by the gain. When we increase pump power, σ_{abs} becomes more negative, the total amount of light leaving the coated nanoparticle increases; i.e., the scattered radiation is accompanied by power being radiated by the active coated nanoparticle. The scattering and absorption efficiencies Q_{scatt} and Q_{abs} are defined as the ratio of the corresponding cross sections σ_{scatt} and σ_{abs} to the geometric cross section of the particle.

By using a computational approach for simulation of plasmonic nanoparticles [34,35], we have calculated the effective scattering, extinction, and absorption cross sections for both Au and Ag nanoparticles and we have found that Ag nanoparticles display significantly larger extinction and scattering cross section than those for Au. Therefore, hereafter we consider Ag-coated nanoparticles with outer diameter $d_{\text{out}} = 48$ nm with active SiO_2 core with inner diameter $d_{\text{in}} = 36$ nm characterized by the optical gain constant $k = -0.1$ that is embedded in poly(methyl methacrylate) (PMMA) ($n_{\text{PMMA}} = 1.495$). In this case, the losses are compensated for by gain, and as a result effective absorption cross section Q_{abs} (magenta solid line) is nearly zero, while scattering and extinction cross sections Q_{scatt} and Q_{ext} coincide (red line); see Fig. 16. When pump power is further increased, i.e., $k = -0.3$—see Fig. 17—one obtains significantly enhanced effective scattering cross section (blue solid line), while both extinction (red dash line) and absorption (magenta dash-dotted line) cross sections become negative, thus indicating outcoming flux power from the active nanoparticle.

[1] A. Kavokin, J. J. Baumberg, G. Malpeuch, and F. P. Laussy, *Microcavities* (Oxford University Press, Oxford, UK, 2007).
[2] J. Kasprzak *et al.*, Nat. Phys. **443**, 409 (2006).
[3] R. Balili, V. Hartwell, D. Snoke, L. Pfeiffer, and K. West, Science **316**, 1007 (2007).
[4] I. Carusotto and C. Ciuti, Phys. Rev. Lett. **93**, 166401 (2004).
[5] A. Amo, D. Sanvitto, F. P. Laussy, D. Ballarini, E. del Valle, M. D. Martin, A. Lemaitre, J. Bloch, D. N. Krizhanovskii, M. S. Skolnick, C. Tejedor, and L. Vina, Nature (London) **457**, 291 (2009).
[6] K. G. Lagoudakis *et al.*, Nat. Phys. **4**, 706 (2008).
[7] K. G. Lagoudakis *et al.*, Science **326**, 974 (2009).
[8] A. Baas, J. P. Karr, H. Eleuch, and E. Giacobino, Phys. Rev. A **69**, 023809 (2004).
[9] N. A. Gippius, S. G. Tikhodeev, V. D. Kulakovskii, D. N. Krizhanovskii, and A. I. Tartakovskii, Europhys. Lett. **67**, 997 (2004).
[10] A. Amo *et al.*, Nat. Photon. **4**, 361 (2010).
[11] D. Sarkar, S. S. Gavrilov, M. Sich, J. H. Quilter, R. A. Bradley, N. A. Gippius, K. Guda, V. D. Kulakovskii, M. S. Skolnick, and D. N. Krizhanovskii, Phys. Rev. Lett. **105**, 216402 (2010).
[12] T. K. Paraïso, M. Wouters, Y. Léger, F. Morier-Genoud, and B. Deveaud-Plédran, Nat. Mater. **9**, 655 (2010).
[13] P. G. Savvidis, J. J. Baumberg, R. M. Stevenson, M. S. Skolnick, D. M. Whittaker, and J. S. Roberts, Phys. Rev. Lett. **84**, 1547 (2000).
[14] Edited by N. Akmediev and A. Ankiewicz, *Dissipative Solitons*, Lecture Notes in Physics 661 (Springer-Verlag, Berlin, Heidelberg, 2005).
[15] T. Ackemann, W. J. Firth, and G.-L. Oppo, in *Advances in Atomic, Molecular and Optical Physics*, edited by E. Arimondo, P. R. Berman, and C. C. Lin (Academic Press, San Diego, CA, 2009), Vol. 57, Chap. 6, pp. 323–421.
[16] K. Staliunas and V. J. Sanchez-Morcillo, *Transverse Patterns in Nonlinear Optical Resonators* (Springer Verlag, Berlin, 2003).
[17] N. N. Rosanov, S. V. Fedorov, P. I. Khadzi, and I. V. Belousov, JETP Lett. **85**, 426 (2007).
[18] A. V. Yulin, O. A. Egorov, F. Lederer, and D. V. Skryabin, Phys. Rev. A **78**, 061801 (2008).
[19] O. A. Egorov, D. V. Skryabin, A. V. Yulin, and F. Lederer, Phys. Rev. Lett. **102**, 153904 (2009).
[20] O. A. Egorov, A. V. Gorbach, F. Lederer, and D. V. Skryabin, Phys. Rev. Lett. **105**, 073903 (2010).
[21] C. M. de Sterke, B. J. Eggleton, and J. E. Sipe, in *Spatial Solitons*, edited by S. Trillo and W. Torruelas (Springer, Berlin, 2001), pp. 169–210.

[22] A. V. Yulin, D. V. Skryabin, and P. St. J. Russel, Phys. Rev. Lett. **91**, 260402 (2003).
[23] K. Staliunas, O. Egorov, Yu. S. Kivshar, and F. Lederer, Phys. Rev. Lett. **101**, 153903 (2008).
[24] K. Staliunas and B. Malomed, Phys. Rev. E **88**, 022917 (2013).
[25] R. H. Ritchie, E. T. Arakawa, J. J. Cowan, and R. N. Hamm, Phys. Rev. Lett. **21**, 1530 (1968).
[26] S. C. Kitson, W. L. Barnes, and J. R. Sambles, Phys. Rev. Lett. **77**, 2670 (1996).
[27] S. I. Bozhevolnyi, J. Erland, K. Leosson, P. M. W. Skovgaard, and J. M. Hvam, Phys. Rev. Lett. **86**, 3008 (2001).
[28] W. L. Barnes, A. Dereux, and T. W. Ebbesen, Nature (London) **424**, 824 (2003).
[29] T. W. Ebbesen, H. J. Lezec, H. F. Ghaemi, T. Thio, and P. A. Wolff, Nature (London) **391**, 667 (1998).
[30] S. Linden, J. Kuhl, and H. Giessen, Phys. Rev. Lett. **86**, 4688 (2001).
[31] E. Cubukcu, K. Aydin, E. Ozbay, S. Foteinopoulou, and C. M. Soukoulis, Nature (London) **423**, 605 (2003).
[32] A. Christ, S. G. Tikhodeev, N. A. Gippius, J. Kuhl, and H. Giessen, Phys. Rev. Lett. **91**, 183901 (2003).
[33] A. Christ, T. Zentgraf, J. Kuhl, S. G. Tikhodeev, N. A. Gippius, and H. Giessen, Phys. Rev. B **70**, 125113 (2004).
[34] U. Hohenester and J. Krenn, Phys. Rev. B **72**, 195429 (2005).
[35] U. Hohenester and A. Trügler, Comp. Phys. Commun. B **183**, 370 (2012).
[36] OptiFDTD 2012 version 11.2, Optiwave Systems Inc.
[37] A. Taflove and S. C. Hagness, *Computational Electromagnetics, The Finite-Difference Time-Domain Method*, 3rd ed. (Artech House, Norwood, MA, 2005).
[38] V. Giannini, Y. Francescato, H. Amrania, Ch. C. Phillips, and S. A. Maier, Nano Lett. **11**, 2835 (2011).
[39] B. Lukyanchuk, N. I. Zheludev, S. A. Maier, N. J. Halas, P. Nordlander, H. Giessen, and C. T. Chong, Nat. Mater. **9**, 707 (2010).
[40] J. A. Gordon and R. Ziolkowski, Opt. Express **15**, 2622 (2007).
[41] E. Desurvire, J. Lightwave Technol. **8**, 1517 (1990).